

1

2 **SPECTRAL COMPUTED TOMOGRAPHY WITH LINEARIZATION
3 AND PRECONDITIONING**

4 YUNYI HU*, MARTIN S. ANDERSEN†, AND JAMES G. NAGY‡

5 **Abstract.** In the area of image sciences, the emergence of spectral computed tomography (CT)
 6 detectors highlights the concept of *quantitative imaging*, in which not only reconstructed images are
 7 offered, but also weights of different materials that compose the object are provided. If a detector is
 8 made up of several energy windows and each energy window is assumed to detect a specific range of
 9 energy spectrum, then a nonlinear matrix equation is formulated to represent the discretized process
 10 of attenuation of x-ray intensity. In this paper, we present a linearization technique to transform this
 11 nonlinear equation into an optimization problem that is based on a weighted least squares term and a
 12 nonnegative bound constraint. To solve this optimization problem, we propose a new preconditioner
 13 that can significantly reduce the condition number, and with this preconditioner, we implement
 14 a highly efficient first order method, Fast Iterative Shrinkage-Thresholding Algorithm (FISTA), to
 15 achieve substantial improvements on convergence speed and image quality. We also use a combination
 16 of generalized Tikhonov regularization and ℓ_1 regularization to stabilize the solution. With the
 17 introduction of new preconditioning, a linear inequality constraint is introduced. In each iteration,
 18 we decompose this constraint into small-sized problems that can be solved with fast optimization
 19 solvers. Numerical experiments illustrate convergence, effectiveness and significance of the proposed
 20 method.

21 **Key words.** preconditioning, digital image reconstruction, FISTA, beam-hardening artifacts,
 22 spectral computed tomography, bound constraints

23 **AMS Subject Classifications:** 65F22, 65F10, 49N45, 65K99

24 **1. Introduction.** The development of new energy-windowed spectral computed
 25 tomography (CT) machines have received a great deal of interest in recent years;
 26 see, e.g. [1, 24]. These detectors assume that x-rays emitted by the x-ray source
 27 are composed of a spectrum of different energies, and in each energy window, the
 28 detector can detect a specific range of energy. Moreover, it assumes that the detector
 29 can perform photon counting and the data collected by the detector are nonnegative
 30 integers. Compared with traditional CT machines, we can avoid introducing beam-
 31 hardening artifacts [19] and improve quality of reconstructed images. To reconstruct
 32 images of an object, we need to solve a nonlinear equation

33 (1.1)
$$\mathbf{Y} = \exp(-\mathbf{A} \mathbf{W} \mathbf{C}^T) \mathbf{S} + \mathbf{\mathcal{E}},$$

34 where \mathbf{Y} is a matrix that gathers the projected data of each energy window in the
 35 corresponding column and the exponential operator is applied element-wise (i.e., it is
 36 not a matrix function). \mathbf{A} is a matrix that is related to the quantitative information
 37 of ray trace and \mathbf{C} is a matrix that contains linear attenuation coefficients for par-
 38 ticular (known) materials at specified energies. \mathbf{S} is the matrix that accumulates the
 39 spectrum energies for each energy window in the corresponding column. We assume
 40 that \mathbf{S} is square and invertible. Moreover, $\mathbf{\mathcal{E}}$ represents the noise term and we assume
 41 that $E_{il} \sim \mathcal{N}(0, y_{il})$ for each component E_{il} in $\mathbf{\mathcal{E}}$ and y_{il} in \mathbf{Y} . We assume that these
 42 data are known and the target is to solve the unknown weight matrix \mathbf{W} . \mathbf{W} is of

*Department of Mathematics and Computer Science, Emory University. Email:
 yhu85@mathcs.emory.edu.

†Department of Applied Mathematics and Computer Science, Technical University of Denmark,
 Email: mskan@dtu.dk.

‡Department of Mathematics and Computer Science, Emory University. Email:
 nagy@mathcs.emory.edu.

43 the size N_v by N_m , where N_v is the number of voxels (pixels if 2D) for each material
 44 map and N_m is the number of materials. Since the weight matrix \mathbf{W} represents the
 45 material maps of different materials, then it must be nonnegative and we need to add
 46 a lower bound $\mathbf{W} \geq \mathbf{0}$.

47 To solve Equation (1.1), we want to vectorize it at first. Then we use the Taylor
 48 expansion to remove the point-wise exponential function and obtain an approximate
 49 linearized equation. Under the Gaussian assumption, as we show in Section 2, we
 50 can transform this equation into a weighted least squares problem under bound con-
 51 straints:

$$52 \quad (1.2) \quad \begin{aligned} \min_{\mathbf{w}} \quad & \frac{1}{2} \|\mathcal{A}\mathbf{w} - \mathbf{b}\|_{\Sigma^{-1}}^2 \\ \text{subject to} \quad & \mathbf{w} \geq \mathbf{0}, \end{aligned}$$

53 where $\mathcal{A} = \mathbf{C} \otimes \mathbf{A}$, $\mathbf{b} = -\log(\mathbf{y})$, $\mathbf{y} = \text{vec}(\mathbf{Y})$ and $\mathbf{w} = \text{vec}(\mathbf{W})$. Σ^{-1} , which
 54 combines information from \mathbf{S} and \mathbf{y} , is the inverse covariance matrix generated by
 55 Gaussian noise and log transformation. $\|\cdot\|_{\Sigma^{-1}}^2$ represents a weighted 2-norm and
 56 $\|\mathcal{A}\mathbf{w} - \mathbf{b}\|_{\Sigma^{-1}}^2 = (\mathcal{A}\mathbf{w} - \mathbf{b})^T \Sigma^{-1} (\mathcal{A}\mathbf{w} - \mathbf{b})$. \mathbf{C} is of the size N_e by N_m , where N_e is
 57 the number of energy and N_m is the number of materials. Since each column of \mathbf{C}
 58 collects the corresponding linear attenuation coefficients and two materials, such as
 59 adipose and glandular, might be similar to each other, the matrix \mathbf{C} is likely to be ill-
 60 conditioned. On the other hand, Problem (1.2) is similar to a quadratic programming
 61 problem under bound constraints. However, direct implementation of an optimization
 62 solver does not provide high-quality reconstruction because the ray trace matrix \mathbf{A} is
 63 large and ill-conditioned, and the columns of the linear attenuation coefficient matrix
 64 \mathbf{C} might be nearly collinear.

65 Because of the ill-posedness, Barber et al. [1] proposed a preconditioner based
 66 on the eigenvalue decomposition of the matrix product of linear attenuation coef-
 67 ficients, $\mathbf{C}^T \mathbf{C}$, to orthogonalize columns of \mathbf{C} . They also suggest using a Poisson
 68 noise assumption and construct loss functions that are either based on the maximum
 69 likelihood estimator (MLE) or the nonlinear least squares term. Using these types of
 70 loss functions and the proposed preconditioner, a *Chambolle-Pock* (CP) primal-dual
 71 method [5] is implemented to solve the corresponding optimization problem. However,
 72 because the MLE for the Poisson model is nonlinear, it is not obvious to see how this
 73 preconditioner can reduce the condition number of the Hessian matrix. Moreover,
 74 because each iteration of a second order method for large three-dimensional imaging
 75 problems is very costly (in terms of both the computations and storage requirements),
 76 in this paper we consider first order methods. With a first order method, it is not
 77 necessary to construct either the Hessian or Hessian-vector multiplication in each step.

78 To mitigate the ill-posedness, we propose a new preconditioner that is based on
 79 a rank-1 approximation of the matrix \mathbf{Y} . With this rank-1 approximation, we can
 80 estimate the Hessian of the objective function in (1.2) by a Kronecker product of two
 81 parts. The first part of this Kronecker product is of the size $N_m \times N_m$, where N_m
 82 denotes the number of materials; usually this is quite small, e.g. $N_m = 2$ or 3 . This
 83 matrix product is also symmetric and positive definite so we can construct a precon-
 84 ditioner from its inverse Cholesky factorization, and thus transform it into an identity
 85 in the preconditioned system. Because the conditioning of the Hessian is closely re-
 86 lated to these two matrices and one of them has been transformed into an identity,
 87 we have reduced the condition number significantly. Moreover, it is an economical
 88 preconditioner since we only need to compute the preconditioner once and can reuse
 89 it in the future iterations. The preconditioner proposed in [1] includes only the data

90 of \mathbf{C} , the matrix of linear attenuation coefficients of material and energy. Compared
 91 with this, the preconditioner proposed in this paper includes the information of linear
 92 attenuation coefficients, the energy spectrum and photon counting data. It offers a
 93 more physically meaningful approximation of the Hessian.

94 In addition, with the weighted least squares objective function, it is much easier
 95 to analyze the condition number before and after preconditioning. Since the per-
 96 formance of a first order method is closely related to the condition number of the
 97 Hessian, it is intuitive to implement a first order method if we can reduce the condi-
 98 tion number significantly. Based on this idea, Fast Iterative Shrinkage-Thresholding
 99 Algorithm (FISTA) [2, 21, 20] comes into view. FISTA is a first order method that
 100 has an “optimal” function convergence rate, $\mathcal{O}(1/k^2)$, where k is the number of iter-
 101 ations. Furthermore, this method is suitable for solving problems that have a form of
 102 $f(\mathbf{x}) + g(\mathbf{x})$ where both $f(\mathbf{x})$ and $g(\mathbf{x})$ are convex but $g(\mathbf{x})$ is possibly nonsmooth.
 103 This $f(\mathbf{x})$ can be the weighted least squares term in Problem (1.2) and $g(\mathbf{x})$ can
 104 represent a nonsmooth regularization term such as ℓ_1 regularization or nonnegative
 105 constraints. Even if we can achieve fast convergence, the introduction of a precon-
 106 ditioner complicates the bound constraints. The previous bound constraints have
 107 become linear inequality constraints because of the preconditioner. However, we can
 108 construct a projection problem that can find the closest solutions to satisfy these
 109 constraints. Moreover, this projection problem is separable and we can apply highly
 110 efficient solvers to compute the solutions to these decomposed small-sized problems.
 111 Generally speaking, the implementations of our preconditioner, FISTA and projec-
 112 tion problem compliment each other and exhibit high-quality reconstructed images
 113 and fast convergence results.

114 This paper is organized as follows. In Section 2, we review the continuous energy-
 115 windowed spectral CT model and the corresponding discretized nonlinear matrix
 116 equation. The linearization, vectorization and set-up of the optimization problem are
 117 also included in Section 2. The key idea of this paper, preconditioning, is introduced
 118 in Section 3. In this section, both the derivation of our preconditioner and an analysis
 119 of the reduction of the condition number are presented. The choice of regularization
 120 will be exhibited in this section as well. In Section 4, we study FISTA and how we
 121 construct and solve the projection problems. Moreover, numerical experiments are
 122 presented in Section 5 and concluding remarks are given in Section 6.

123 **2. The Energy-windowed Spectral CT Model.** In this section, we start
 124 with an introduction to the basic model. Then we show how to discretize this model
 125 to obtain a matrix equation. Since we do not want to solve this matrix equation
 126 directly, we therefore vectorize this equation and take the Taylor expansion to the
 127 first order term to remove the exponential function. In this case, we can obtain a
 128 linear system with transformed noise. With this transformed noise, we can build a
 129 weighted least squares optimization problem under bound constraints.

130 In computed tomography (CT), source x-ray beams are composed of a spectrum
 131 of different energies [4]. Recent technological developments have resulted in the de-
 132 sign of new photon counting detectors that can discriminate the measured data into
 133 specific energy windows. Image reconstruction algorithms that exploit this informa-
 134 tion can avoid introducing beam-hardening artifacts, obtain material decomposition
 135 and improve the quality of reconstructed images. The mathematical model for image
 136 reconstruction uses Beer’s law [12], which states that the change of x-ray intensity

137 before and after illumination through the object is

$$(2.1) \quad 138 \quad y_i^{(k)} = \int_E S^{(k)}(e) \exp \left(- \int_{t \in l} \mu(\vec{r}(t), e) dt \right) de + \eta_i^{(k)}, \quad \begin{cases} i = 1, 2, \dots, N_d \times N_p, \\ k = 1, 2, \dots, N_b, \end{cases}$$

139 where

- 140 • $y_i^{(k)}$ is x-ray intensity of the i -th pixel in the k -th detector bin.
- 141 • E is the photon flux density. Figure 5.2 shows a curve of E versus photon energy.
- 143 • N_d is the number of detector pixels. For a material map of the size n by n , we assume $N_d = n$.
- 145 • N_p is the number of projections. For cone/fan beam CT, projections are uniformly distributed from 0 to 360 degrees.
- 147 • N_b is the number of detector bins. For an energy-windowed CT machine, we usually assume that it has 5 to 6 energy bins.
- 149 • $S^{(k)}(e)$ represents photon flux density for the k -th detector bin, which is the number of incident photons at the energy e in the k -th energy window.
- 151 • $\mu(\vec{r}(t), e)$ denotes the linear attenuation coefficient that is related to the position function $\vec{r}(t)$ and the energy level e .
- 153 • $\eta_i^{(k)}$ is the error term for the i -th element in the k -th energy bin and it is assumed to be Gaussian for this model.

155 In Equation (2.1), the unknown linear attenuation coefficient $\mu(\vec{r}(t), e)$ is dependent on the position function $r(t)$ and the energy levels e . If the object is assumed to be composed of several different materials, then a material expansion is introduced to further decompose the function $\mu(\vec{r}(t), e)$ [11]:

$$159 \quad (2.2) \quad \mu(\vec{r}(t), e) = \sum_{m=1}^{N_m} u_{m,e} w_m(\vec{r}),$$

160 where

- 161 • N_m is the number of materials that form the object.
- 162 • $u_{m,e}$ is the linear attenuation coefficient for the m -th material at the energy level e .
- 164 • $w_m(\vec{r})$ is the unknown weight of the m -th material at the position \vec{r} .
- 165 With this decomposition, the unknown variable has been shifted from $\mu(\vec{r}(t), e)$ to the weight fraction $w_m(\vec{r})$. If we also assume that $w_m(\vec{r})$ can be represented as a 166 sum of product of weights and basis functions $\phi_j(\vec{r})$, then another expansion can be 167 expressed by

$$169 \quad (2.3) \quad w_m(\vec{r}) = \sum_{j=1}^{N_v} w_{j,m} \phi_j(\vec{r}),$$

170 where

- 171 • N_v is the number of voxels (pixels if 2D) of images that compose the object.
- 172 • $w_{j,m}$ is the weight fraction of the m -th material in the j -th voxel (pixels if 173 2D).
- 174 • $\phi_j(\vec{r})$ is the basis function of image representation. The line integral of the 175 basis function, $a_{i,j}$, is the length of the x-ray beam through the j -th voxel 176 (pixel if 2D), incident onto the i -th element of the product of detector pixels

177 N_d and the number of projections N_p :

178 (2.4)
$$a_{i,j} = \int_{t \in l} \phi_j(\vec{r}(t)) dt.$$

179 Then the line integral in Equation (2.1) can be simplified by Expansion (2.3) and
180 Integral (2.4):

181 (2.5)
$$\int_{t \in l} \mu(\vec{r}(t), e) dt = \sum_{m=1}^{N_m} \sum_{j=1}^{N_v} u_{m,e} w_{j,m} \int_{t \in l} \phi_j(\vec{r}(t)) dt = \sum_{j=1}^{N_v} \sum_{m=1}^{N_m} a_{i,j} w_{j,m} u_{m,e}.$$

182 If we also discretize the integral over the energy E and ignore quadrature errors, then
183 the discrete model of Equation (2.1) can be written as:

184 (2.6)
$$y_i^{(k)} = \sum_{e=1}^{N_e} s_e^{(k)} \exp \left(- \sum_{j=1}^{N_v} \sum_{m=1}^{N_m} a_{i,j} w_{j,m} u_{m,e} \right) + \eta_i^{(k)},$$

185 where N_e is the number of discrete energies. If we collect $a_{i,j}$, $w_{i,j}$ and $u_{m,e}$ in a
186 matrix form and concatenate $y_i^{(k)}$, $s_e^{(k)}$, $\eta_i^{(k)}$ with respect to their energy windows,
187 then the corresponding matrix equation of (2.6) can be represented as:

188 (2.7)
$$\mathbf{Y} = \exp(-\mathbf{A} \mathbf{W} \mathbf{C}^T) \mathbf{S} + \mathbf{\mathcal{E}},$$

189 where

- 190 • \mathbf{Y} is a matrix of the size $(N_d \cdot N_p) \times N_b$ that gathers x-ray photons of each
191 energy window in the corresponding column.
- 192 • \mathbf{A} is a matrix of the size $(N_d \cdot N_p) \times N_v$ that collects the fan-beam geometry
193 and each element corresponds to $a_{i,j}$.
- 194 • \mathbf{C} is a matrix of the size $N_e \times N_m$ that accumulates linear attenuation
195 coefficients and each entry corresponds to $u_{e,m}$, the linear attenuation coefficient
196 of the energy e and the m -th material.
- 197 • \mathbf{S} is a matrix of the size $N_e \times N_b$ and each column collects the spectrum
198 energy of a specific range. In the forward problem, we use the full spectrum,
199 but when we solve the inverse problem, the average in each energy window
200 is used to represent the corresponding spectral energy. Therefore, $N_b = N_e$
201 for the inverse problem and \mathbf{S} is an invertible diagonal matrix because the
202 means are placed in the diagonal. A detailed example is shown in Figure 5.2.
- 203 • $\mathbf{\mathcal{E}}$ is the noise matrix that is of the size $(N_d \cdot N_p) \times N_b$. The assumption for
204 the noise is $E_{il} \sim \mathcal{N}(0, y_{il})$ for each element E_{il} in $\mathbf{\mathcal{E}}$ and y_{il} in \mathbf{Y} .

205 In Equation (2.7), the exponential operator is applied element-wise (i.e., it is not a
206 matrix function). In addition to Equation (2.7), we also require that weight fractions
207 should be nonnegative and this can be illustrated by the constraint $\mathbf{W} \geq \mathbf{0}$.

208 In several cases, the composition of materials can be similar. For example, glan-
209 dular and adipose have similar attenuation coefficients at the same energy level and
210 it causes the collinearity. After discretization, the columns of \mathbf{C} can be nearly de-
211 pendent. Moreover, \mathbf{A} is large-scale and sparse and it is highly likely to have small
212 singular values. As we will see later, the Hessian system involves the Kronecker prod-
213 uct $\mathbf{C} \otimes \mathbf{A}$ and it can cause the ill-posedness. Since it is challenging to solve this
214 equation directly, it is important to consider approaches to facilitate the process.
215 First, we can introduce a preconditioning matrix \mathbf{M} into Equation (2.7):

216 (2.8)
$$\mathbf{Y} = \exp(-\mathbf{A} \mathbf{W} \mathbf{M}^{-T} \mathbf{M}^T \mathbf{C}^T) \mathbf{S} + \mathbf{\mathcal{E}}.$$

217 If we let $\tilde{\mathbf{W}} = \mathbf{W}\mathbf{M}^{-T}$ and $\tilde{\mathbf{C}} = \mathbf{C}\mathbf{M}$, then Equation (2.8) is equivalent to

218 (2.9)
$$\mathbf{Y} = \exp(-\mathbf{A}\tilde{\mathbf{W}}\tilde{\mathbf{C}}^T) \mathbf{S} + \boldsymbol{\varepsilon}.$$

219 So far, we have not introduced how to choose the preconditioner \mathbf{M} . The choice of \mathbf{M}
220 depends on linearization and approximation. In Section (3.1), we will state the process
221 in detail, and in the new coordinate system defined by \mathbf{M} , the corresponding Hessian
222 will be better conditioned. With the help of the preconditioning matrix \mathbf{M} , we have
223 transformed the original system of solving \mathbf{W} into the new system of solving $\tilde{\mathbf{W}}$.
224 Since each entry of $\tilde{\mathbf{W}}$ is a linear combination of all entries in the corresponding row
225 of \mathbf{W} , we can try to find a matrix \mathbf{M} such that the new system is better conditioned
226 than the original one.

227 On the other hand, we do not want to solve the nonlinear matrix equation (2.9)
228 directly because it might introduce a tensor when we compute second order derivatives.
229 In this case, we want to vectorize Equation (2.9) on both sides and linearize it
230 to construct a weighted least squares optimization problem. In the forward problem,
231 we use the full spectrum and the matrix \mathbf{S} is then usually rectangular. When we
232 solve the inverse problem, we choose the average in each energy window to represent
233 the corresponding energy spectrum. In this case, $N_b = N_e$ and the matrix \mathbf{S} in the
234 inverse problem is a nonsingular diagonal matrix. So we can multiply \mathbf{S}^{-1} on both
235 sides of (2.9):

236 (2.10)
$$\mathbf{Y}\mathbf{S}^{-1} = \exp(-\mathbf{A}\tilde{\mathbf{W}}\tilde{\mathbf{C}}^T) + \boldsymbol{\varepsilon}\mathbf{S}^{-1}.$$

237 Vectorizing both sides of (2.10), and using properties of Kronecker products, we obtain

238 (2.11)
$$(\mathbf{S}^{-T} \otimes \mathbf{I}) \mathbf{y} = \exp\left\{-\left(\tilde{\mathbf{C}} \otimes \mathbf{A}\right) \tilde{\mathbf{w}}\right\} + (\mathbf{S}^{-T} \otimes \mathbf{I}) \mathbf{e},$$

239 where $\mathbf{y} = \text{vec}(\mathbf{Y})$, $\tilde{\mathbf{w}} = \text{vec}(\tilde{\mathbf{W}})$ and $\mathbf{e} = \text{vec}(\mathbf{E})$. If we let $\tilde{\mathbf{y}} = (\mathbf{S}^{-T} \otimes \mathbf{I}) \mathbf{y}$ and
240 $\tilde{\mathbf{e}} = (\mathbf{S}^{-T} \otimes \mathbf{I}) \mathbf{e}$, then we can subtract $\tilde{\mathbf{e}}$ on both sides of (2.11) and obtain

241 (2.12)
$$\tilde{\mathbf{y}} - \tilde{\mathbf{e}} = \exp\left\{-\left(\tilde{\mathbf{C}} \otimes \mathbf{A}\right) \tilde{\mathbf{w}}\right\}.$$

242 By taking the logarithm on both sides of Equation (2.12), we can obtain a linear
243 equation

244 (2.13)
$$\log(\tilde{\mathbf{y}} - \tilde{\mathbf{e}}) = -\left(\tilde{\mathbf{C}} \otimes \mathbf{A}\right) \tilde{\mathbf{w}}.$$

245 However, the left-hand side of Equation (2.13) contains the transformed error term $\tilde{\mathbf{e}}$
246 so we cannot solve this equation directly. In this case, we can separate the error term
247 $\tilde{\mathbf{e}}$ from $\tilde{\mathbf{y}}$ using a first order Taylor expansion at $\tilde{\mathbf{y}}$:

248 (2.14)
$$\log(\tilde{\mathbf{y}} - \tilde{\mathbf{e}}) = \log(\tilde{\mathbf{y}}) - \text{diag}(\tilde{\mathbf{y}})^{-1} \tilde{\mathbf{e}} + \mathcal{O}(\|\tilde{\mathbf{e}}\|_2^2).$$

249 If we use the first two terms on the right-hand side of Equation (2.14) to estimate
250 the term $\log(\tilde{\mathbf{y}} - \tilde{\mathbf{e}})$, then Equation (2.13) can be expressed by a linear equation with
251 the error term $\text{diag}(\tilde{\mathbf{y}})^{-1} \tilde{\mathbf{e}}$. Let $\mathbf{b} = -\log(\tilde{\mathbf{y}})$, then Equation (2.13) is approximately
252 equal to

253 (2.15)
$$\mathbf{b} \approx \left(\tilde{\mathbf{C}} \otimes \mathbf{A}\right) \tilde{\mathbf{w}} - \text{diag}(\tilde{\mathbf{y}})^{-1} \tilde{\mathbf{e}}.$$

254 With this equation and the Gaussian assumption of noise $\mathbf{e} \sim \mathcal{N}(\mathbf{0}, \text{diag}(\mathbf{y}))$, we
255 have

256 (2.16)
$$\mathbf{b}|\tilde{\mathbf{w}} \sim \mathcal{N}\left(\left(\tilde{\mathbf{C}} \otimes \mathbf{A}\right) \tilde{\mathbf{w}}, \Sigma\right),$$

257 where the noise covariance matrix Σ is expressed by

258 (2.17)
$$\Sigma = \text{diag}(\tilde{\mathbf{y}})^{-1} (\mathbf{S}^{-T} \otimes \mathbf{I}) \text{diag}(\mathbf{y}) (\mathbf{S}^{-1} \otimes \mathbf{I}) \text{diag}(\tilde{\mathbf{y}})^{-1},$$

259 and the inverse covariance matrix is given by

260 (2.18)
$$\Sigma^{-1} = \text{diag}(\tilde{\mathbf{y}}) (\mathbf{S} \otimes \mathbf{I}) \text{diag}(\mathbf{y})^{-1} (\mathbf{S}^T \otimes \mathbf{I}) \text{diag}(\tilde{\mathbf{y}}).$$

261 Since \mathbf{Y} is a matrix that collects the number of photons of each energy window in the
262 corresponding column, each entry of \mathbf{Y} is a positive integer whose value can be in the
263 order of hundreds of thousands. As long as the noise does not dominate the projected
264 data, we expect the entries of $\tilde{\mathbf{y}}$ will be larger than zero. From Expression (2.18), we
265 can see that the structure of Σ^{-1} depends on the structure of the matrix \mathbf{S} . If \mathbf{S} is
266 diagonal, then Σ is also diagonal. If we let $\mathcal{A} = \tilde{\mathbf{C}} \otimes \mathbf{A}$, then (see, e.g., [3]) the best
267 unbiased linear estimator of $\tilde{\mathbf{w}}$ for the Gaussian model (2.16) is the solution of

268 (2.19)
$$\min_{\tilde{\mathbf{w}}} \frac{1}{2} (\mathcal{A} \tilde{\mathbf{w}} - \mathbf{b})^T \Sigma^{-1} (\mathcal{A} \tilde{\mathbf{w}} - \mathbf{b}).$$

269 In addition, we require that $\mathbf{W} \geq \mathbf{0}$, and with the preconditioner, these constraints
270 are transformed into $(\mathbf{M} \otimes \mathbf{I}) \tilde{\mathbf{w}} \geq \mathbf{0}$. Therefore, we can formulate a weighted least
271 squares problem under bound constraints

272 (2.20)
$$\begin{aligned} \min_{\tilde{\mathbf{w}}} \quad & \frac{1}{2} \|\mathcal{A} \tilde{\mathbf{w}} - \mathbf{b}\|_{\Sigma^{-1}}^2 \\ \text{subject to} \quad & (\mathbf{M} \otimes \mathbf{I}) \tilde{\mathbf{w}} \geq \mathbf{0}. \end{aligned}$$

273 In (2.20) the norm $\|\cdot\|_{\Sigma^{-1}}^2$ corresponds to the weighted inner product given in (2.19).
274 From this expression, we know that the objective function is convex. Moreover, the
275 inverse covariance matrix Σ^{-1} is diagonal as long as \mathbf{S} is diagonal and this optimiza-
276 tion problem has linear inequality constraints. Based on these observations, we can
277 identify four challenges involved in solving this optimization problem. At first, we
278 need to choose an appropriate preconditioning matrix to reduce the ill-conditioning
279 of the Hessian. Secondly, we want to select suitable regularizations for the correspond-
280 ing materials. Thirdly, we have to find an efficient method to solve the constrained
281 weighted least squares problem. These three challenges are related to each other and
282 an appropriate preconditioner with appropriate regularizations will be beneficial for
283 the solver efficiency. Finally, we should handle linear inequality constraints in an
284 efficient way. We will address these four challenges in the following sections.

285 **3. Preconditioning and Regularization.**

286 **3.1. Preconditioning.** The choice of the preconditioning matrix \mathbf{M} is crucial for
287 solving the optimization problem (2.20). If we do not have a preconditioner or we
288 choose the preconditioner \mathbf{M} as identity, the original Hessian for the weighted least
289 squares problem (2.20) is expressed by

290 (3.1)
$$\mathbf{H} = (\mathbf{C}^T \otimes \mathbf{A}^T) \Sigma^{-1} (\mathbf{C} \otimes \mathbf{A}).$$

291 An appropriate preconditioner can transform the original ill-posed system into a
 292 better-conditioned system and thus bring faster convergence speed as well as higher
 293 quality of reconstructed images. In general, the preconditioned Hessian $\tilde{\mathbf{H}}$ can be
 294 represented as

295 (3.2)
$$\tilde{\mathbf{H}} = \mathcal{A}^T \Sigma^{-1} \mathcal{A} = (\tilde{\mathbf{C}}^T \otimes \mathbf{A}^T) \Sigma^{-1} (\tilde{\mathbf{C}} \otimes \mathbf{A}),$$

296 where $\tilde{\mathbf{C}} = \mathbf{C}\mathbf{M}$. From this expression, it is still not obvious how to construct the
 297 preconditioner. However, if we can separate the noise covariance matrix Σ^{-1} into a
 298 Kronecker product of two terms, we can merge several terms using properties of the
 299 Kronecker product and transform parts of the Hessian into identity with the help of
 300 \mathbf{M} . To realize this idea, we review the expression of Σ^{-1} in Equation (2.18), where
 301 we can see that it contains the Kronecker products $\mathbf{S} \otimes \mathbf{I}$ and $\mathbf{S}^T \otimes \mathbf{I}$ and it is not
 302 necessary to separate these two terms. So we focus on the other terms that include
 303 $\text{diag}\{\tilde{\mathbf{y}}\}$ and $\text{diag}\{\mathbf{y}\}^{-1}$. By definition, these two terms are related to each other by
 304 $\tilde{\mathbf{y}} = (\mathbf{S}^{-T} \otimes \mathbf{I}) \mathbf{y}$. In this case, if we can express $\text{diag}\{\mathbf{y}\}$ into a Kronecker product
 305 of two terms, then we will reach the goal.

306 Recall that $\mathbf{y} = \text{vec}(\mathbf{Y})$. Therefore, if we can find two rank-1 matrices, \mathbf{u} and \mathbf{v} ,
 307 such that $\mathbf{Y} \approx \mathbf{u}\mathbf{v}^T$, then

308 (3.3)
$$\text{diag}\{\mathbf{y}\} \approx \text{diag}\{\text{vec}(\mathbf{u}\mathbf{v}^T)\} = \text{diag}\{\mathbf{v}\} \otimes \text{diag}\{\mathbf{u}\}.$$

309 These two rank-1 matrices can be obtained by solving a nearest Kronecker product
 310 (NKP) problem, which is equivalent to a rank-1 approximation of \mathbf{Y} in terms of the
 311 Frobenius norm:

312 (3.4)
$$\min_{\mathbf{u}, \mathbf{v}} \|\mathbf{Y} - \mathbf{u}\mathbf{v}^T\|_F.$$

313 The solution to this problem has been studied extensively [23]. Using the singular
 314 value decomposition (SVD), one solution to Problem (3.4) can be expressed by $\mathbf{u} =$
 315 $\sqrt{\sigma_1} \mathbf{u}_1$ and $\mathbf{v} = \sqrt{\sigma_1} \mathbf{v}_1$, where \mathbf{u}_1 and \mathbf{v}_1 are the first left and right singular vectors
 316 and σ_1 is the corresponding largest singular value of \mathbf{Y} . Since we only need these
 317 terms rather than a full SVD, we can use MATLAB's `svds` function, or other efficient
 318 approaches, such as "PROPACK" [14], to calculate only σ_1 , \mathbf{u}_1 and \mathbf{v}_1 .

319 After we have obtained \mathbf{u} and \mathbf{v} , we can estimate the matrix $\text{diag}\{\mathbf{y}\}$ as a Kro-
 320 necker product of two terms as Equation (3.3). In addition, the term $\text{diag}\{\tilde{\mathbf{y}}\}$ can be
 321 represented as

322 (3.5)
$$\begin{aligned} \text{diag}\{\tilde{\mathbf{y}}\} &= \text{diag}\{(\mathbf{S}^{-T} \otimes \mathbf{I}) \text{vec}(\mathbf{Y})\} \approx \text{diag}\{(\mathbf{S}^{-T} \otimes \mathbf{I}) \text{vec}(\mathbf{u}\mathbf{v}^T)\} \\ &= \text{diag}\{\text{vec}(\mathbf{u}\mathbf{v}^T \mathbf{S}^{-1})\} = \text{diag}\{\mathbf{S}^{-T} \mathbf{v}\} \otimes \text{diag}\{\mathbf{u}\}. \end{aligned}$$

323 If we substitute the terms in (3.3) and (3.5) for the same terms in (2.18), we can
 324 obtain that

325 (3.6)
$$\Sigma^{-1} \approx \left(\text{diag}\{\mathbf{S}^{-T} \mathbf{v}\} \mathbf{S} \text{diag}\{\mathbf{v}\}^{-1} \mathbf{S}^T \text{diag}\{\mathbf{S}^{-T} \mathbf{v}\} \right) \otimes \text{diag}\{\mathbf{u}\}.$$

326 So the preconditioned Hessian matrix is given by

(3.7)
$$\begin{aligned} \tilde{\mathbf{H}} &= (\tilde{\mathbf{C}}^T \otimes \mathbf{A}^T) \Sigma^{-1} (\tilde{\mathbf{C}} \otimes \mathbf{A}) \\ &\approx (\tilde{\mathbf{C}}^T \otimes \mathbf{A}^T) \left[\text{diag}\{\mathbf{S}^{-T} \mathbf{v}\} \mathbf{S} \text{diag}\{\mathbf{v}\}^{-1} \mathbf{S}^T \text{diag}\{\mathbf{S}^{-T} \mathbf{v}\} \otimes \text{diag}\{\mathbf{u}\} \right] (\tilde{\mathbf{C}} \otimes \mathbf{A}) \\ &= (\tilde{\mathbf{C}}^T \text{diag}\{\mathbf{S}^{-T} \mathbf{v}\} \mathbf{S} \text{diag}\{\mathbf{v}\}^{-1} \mathbf{S}^T \text{diag}\{\mathbf{S}^{-T} \mathbf{v}\} \tilde{\mathbf{C}}) \otimes (\mathbf{A}^T \text{diag}\{\mathbf{u}\} \mathbf{A}). \end{aligned}$$

328 Since the size of $\tilde{\mathbf{C}}$ is $N_e \times N_m$, then the first part of the Kronecker product in
 329 (3.7) is a square matrix of the size $N_m \times N_m$. In other words, this part only de-
 330 pends on the number of materials that compose the object. Usually, we only con-
 331 sider 2 or 3 materials for the object so that the size of the matrix products for this
 332 part is usually either 2×2 or 3×3 . Moreover, the matrix \mathbf{Y} gathers the num-
 333 ber of photons of each energy window in the corresponding column so all of its en-
 334 tries are positive integers. In this case, we can choose \mathbf{u} and \mathbf{v} to be positive such
 335 that $\mathbf{C}^T \text{diag}\{\mathbf{S}^{-T} \mathbf{v}\} \mathbf{S} \text{diag}\{\mathbf{v}\}^{-1} \mathbf{S}^T \text{diag}\{\mathbf{S}^{-T} \mathbf{v}\} \mathbf{C}$ is a symmetric positive definite
 336 (SPD) matrix. Therefore, we can calculate \mathbf{M} with the Cholesky decomposition:

337 (3.8)
$$\mathbf{C}^T \text{diag}\{\mathbf{S}^{-T} \mathbf{v}\} \mathbf{S} \text{diag}\{\mathbf{v}\}^{-1} \mathbf{S}^T \text{diag}\{\mathbf{S}^{-T} \mathbf{v}\} \mathbf{C} = \mathbf{G}^T \mathbf{G},$$

338 where \mathbf{G} is an upper triangular matrix with positive diagonal entries. Since $\tilde{\mathbf{C}} = \mathbf{C} \mathbf{M}$,
 339 we can choose $\mathbf{M} = \mathbf{G}^{-1}$ to transform this part into identity. From Expression (3.7),
 340 we see that the preconditioned Hessian, $\tilde{\mathbf{H}}$, is dependent on a Kronecker product of
 341 two parts and the first part has been transformed into an identity. In particular,
 342 since the condition number of this part is typically significantly greater than 1, the
 343 condition number of the preconditioned Hessian $\tilde{\mathbf{H}}$ is significantly smaller than the
 344 original Hessian \mathbf{H} .

345 After we have obtained the matrix \mathbf{M} , we can analyze the effect of preconditioning
 346 using the SVD. Without preconditioning, the Hessian matrix \mathbf{H} depends on two parts,
 347 $\mathbf{C}^T \text{diag}\{\mathbf{S}^{-T} \mathbf{v}\} \mathbf{S} \text{diag}\{\mathbf{v}\}^{-1} \mathbf{S}^T \text{diag}\{\mathbf{S}^{-T} \mathbf{v}\} \mathbf{C}$ and $\mathbf{A}^T \text{diag}\{\mathbf{u}\} \mathbf{A}$. If we assume
 348 the singular value decomposition for these two matrices are $\mathbf{U}_1 \boldsymbol{\Sigma}_1 \mathbf{V}_1^T$ and $\mathbf{U}_2 \boldsymbol{\Sigma}_2 \mathbf{V}_2^T$,
 349 then the condition number of the original Hessian \mathbf{H} is closely related to $\boldsymbol{\Sigma}_1$ and $\boldsymbol{\Sigma}_2$.
 350 Let the largest and smallest singular values of $\boldsymbol{\Sigma}_1$ and $\boldsymbol{\Sigma}_2$ be σ_{1max} , σ_{1min} , σ_{2max} and
 351 σ_{2min} , respectively, then the condition number of the original Hessian, $\kappa(\mathbf{H})$, can be
 352 estimated as

353 (3.9)
$$\kappa(\mathbf{H}) = \frac{\sigma_{1max} \sigma_{2max}}{\sigma_{1min} \sigma_{2min}}.$$

354 On the other hand, the condition number of the preconditioned Hessian can be ap-
 355 proximated by

356 (3.10)
$$\kappa(\tilde{\mathbf{H}}) = \frac{\sigma_{2max}}{\sigma_{2min}}.$$

357 Since the fraction $\sigma_{1max}/\sigma_{1min}$ is most likely to be significantly greater than 1, the
 358 condition number of $\tilde{\mathbf{H}}$ is likely to be much smaller than \mathbf{H} . To validate this phe-
 359 nomenon, we can build a numerical example to compare the condition numbers. For
 360 an object that is composed of two materials and each material map is of the size
 361 16×16 , we can construct the original Hessian \mathbf{H} and the preconditioned Hessian $\tilde{\mathbf{H}}$
 362 explicitly and compute the estimations of condition numbers for these two Hessian
 363 matrices. The result is presented in Table 3.1. From Table 3.1, we can see that the

Matrix Types	Condition Numbers
Original Hessian	2.00 e+06
Preconditioned Hessian	2.59 e+04

TABLE 3.1
Comparison of Condition Numbers

364 difference between $\kappa(\mathbf{H})$ and $\kappa(\tilde{\mathbf{H}})$ is around two orders of magnitude, which indicates the significance of this preconditioner. For a linear system that involves the 365 preconditioned Hessian $\tilde{\mathbf{H}}$, the convergence rate is highly dependent on the condition 366 number. With a better-conditioned system, we can compute the solution in a more 367 efficient way. Moreover, we will validate the strength of this preconditioner by solving 368 the preconditioned system versus the original system. More details are presented in 369 Section 5.

371 **3.2. Regularization.** With the help of our preconditioner, we can speed up an 372 optimization algorithm and achieve higher accuracy. To further alleviate the noise 373 amplification, it is important to add regularization terms to the objective function. 374 In total, we have m materials and the weights of these m materials are not equal. 375 Rather than adding a single regularization to all weights, we should add a specific 376 regularization to each material. In addition, for different materials, we can choose dis- 377 tinct regularizations to match their properties. For the dominant material, we select 378 the generalized Tikhonov regularization to smooth the edges. For other materials, we 379 choose the ℓ_1 regularization to penalize the sum of weights. Based on this idea, we 380 can represent the regularization term as a sum of m parts:

$$381 \quad (3.11) \quad R(\mathbf{w}) = \sum_{i=1}^m \frac{\alpha_i}{2} R_i(\mathbf{w}_i),$$

382 where \mathbf{w}_i is the vectorization form of the i -th weight matrix, $R_i(\mathbf{w}_i)$ is the corre- 383 sponding regularization term and α_i is the regularization parameter.

384 The choice of what type of regularization to use is problem-specific, and *a priori* 385 knowledge of the object being imaged could inform this decision. For example, if it is 386 known that the object contains two material maps with relatively equal distributions, 387 we might select two generalized Tikhonov regularizations. In breast imaging, if the 388 object is dominated by glandular and adipose tissue, it might make sense to use a 389 generalized Tikhonov regularization for each of them. On the other hand, it could be 390 the case that the object is dominated by one material (or one set of materials), with a 391 relatively sparse distribution of another material. In the breast imaging situation, the 392 object may contain small micro-calcifications or areas highlighted by an iodine tracer. 393 In this case, one can use generalized Tikhonov regularizations for the dominating 394 materials (e.g., glandular and adipose tissue) and an ℓ_1 regularization for the sparse 395 material. We illustrate this with two materials, one that dominates, and one that is 396 sparse:

$$397 \quad (3.12) \quad R(\mathbf{w}) = \frac{\alpha_1}{2} \|\mathbf{L}\mathbf{w}_1\|_2^2 + \frac{\alpha_2}{2} \|\mathbf{w}_2\|_1.$$

398 If we add these regularization terms to the objective function in Equation (2.20), we 399 can rewrite it as an augmented system:

$$400 \quad (3.13) \quad \min_{\tilde{\mathbf{w}}} \quad \left\| \begin{bmatrix} \frac{\sqrt{2}}{2} \Sigma^{-\frac{1}{2}} (\tilde{\mathbf{C}} \otimes \mathbf{A}) \\ \sqrt{\frac{\alpha_1}{2}} \tilde{\mathbf{L}} \end{bmatrix} \tilde{\mathbf{w}} - \begin{bmatrix} \Sigma^{-\frac{1}{2}} \mathbf{b} \\ \mathbf{0} \end{bmatrix} \right\|_2^2 + \frac{\alpha_2}{2} [\mathbf{0} \quad \mathbf{1}] (\mathbf{M} \otimes \mathbf{I}) \tilde{\mathbf{w}}$$

subject to $(\mathbf{M} \otimes \mathbf{I}) \tilde{\mathbf{w}} \geq \mathbf{0}$,

401 where $\tilde{\mathbf{L}} = [\mathbf{L} \quad \mathbf{0}] (\mathbf{M} \otimes \mathbf{I})$. As we can see, the objective function in this problem 402 consists of two parts: one is smooth and convex and the other one is possibly non- 403 smooth. Because of these properties, we can think about using FISTA [2] to solve

404 this problem. It not only fits the features of the objective function but also provides an optimal convergence rate. In addition, we are concerned about the linear
 405 inequality constraints, and in each step, we can maintain these constraints by solving
 406 a projection problem that is based on the 2-norm.
 407

408 **4. FISTA and Projections.** In this section, we first briefly present the main
 409 algorithm FISTA. To implement FISTA to solve the target optimization problem, we
 410 need to determine the step size and handle the nonnegative constraints. For the step
 411 size, we introduce how to compute the Lipschitz constant numerically and then choose
 412 a constant step size based on the calculated Lipschitz constant. For the nonnegative
 413 constraints, we build another quadratic programming problem and solve it with a
 414 delicate decomposition and efficient algorithms.

415 **4.1. FISTA.** Fast Iterative Shrinkage-Thresholding Algorithm (FISTA) is a first
 416 order method that belongs to the family of Iterative Shrinkage-Thresholding Algo-
 417 rithm (ISTA). This method is proposed by Beck et al., and compared with the $\mathcal{O}(1/k)$
 418 rate of convergence of ISTA, it has a best function value convergence rate $\mathcal{O}(1/k^2)$,
 419 where k is the number of iterations. Moreover, it is very appropriate for problems in
 420 imaging science because it is usually used to solve the nonsmooth convex problem

421 (4.1)
$$\min_{\mathbf{x}} f(\mathbf{x}) + g(\mathbf{x}),$$

422 where $f(\mathbf{x})$ and $g(\mathbf{x})$ are both convex functions and $g(\mathbf{x})$ might not be smooth. In
 423 imaging sciences, $f(\mathbf{x})$ is likely to be a least squares loss function to test the goodness
 424 of fit and $g(\mathbf{x})$ can be a regularization term such as a ℓ_1 penalty or a total variation
 425 regularization. For Problem (3.13), we construct an augmented loss function that
 426 merges the generalized Tikhonov regularization term, which corresponds to $f(\mathbf{x})$ in
 427 (4.1). For the regularization term, the ℓ_1 regularization is nonsmooth but convex and
 428 this matches $g(\mathbf{x})$ in (4.1).

429 The details of this algorithm are shown in Algorithm (4.1). For the main algo-
 430 rithm, we need to compute the smallest Lipschitz constant K at first. Then we can
 431 update the current step using FISTA. Because of the linear inequality constraints, we
 432 need to project the new step onto these constraints to keep the solution feasible. We

Algorithm 4.1 FISTA and Projections [2]

- 1: *Initialization:*
- 2: Calculate the smallest Lipschitz constant K in (4.3) by Power Method.
- 3: Set up the initial guess $\tilde{\mathbf{W}}_0$; Let $\mathbf{y}_0 = \text{vec}(\tilde{\mathbf{W}}_0)$, $\mathbf{x}_{old} = \mathbf{y}_0$ and $t_1 = 1$;
- 4: **for** $k = 1, 2, \dots$ **do**
- 5: Calculate the gradients, $\nabla f(\mathbf{y}_k)$ and $\nabla g(\mathbf{y}_k)$, of $f(\mathbf{y}_k)$ and $g(\mathbf{y}_k)$ in (4.2);
- 6: $\mathbf{x}_k = \mathbf{y}_k - \frac{1}{L(f)} [\nabla f(\mathbf{y}_k) + \nabla g(\mathbf{y}_k)];$
- 7: Reshape \mathbf{x}_k into a matrix and use CVXGEN to solve the projection problems
 to obtain \mathbf{x}_{new} as (4.6);
- 8: $t_{k+1} = \frac{1 + \sqrt{1 + 4t_k^2}}{2};$
- 9: $\mathbf{y}_{k+1} = \mathbf{x}_{new} + \left(\frac{t_k - 1}{t_{k+1}} \right) (\mathbf{x}_{new} - \mathbf{x}_{old});$
- 10: $\mathbf{x}_{old} = \mathbf{x}_{new}.$

432 would like to implement FISTA with a constant step size to solve the optimization
 433 problem (3.13). To implement this method, we need several preparations, which we
 434 will discuss in the following sections.
 435

436 **4.2. Lipschitz Constant.** The first step is to calculate the smallest Lipschitz
 437 constant. If we let

$$438 \quad (4.2) \quad f(\tilde{\mathbf{w}}) = \left\| \begin{bmatrix} \frac{\sqrt{2}}{2} \Sigma^{-\frac{1}{2}} (\tilde{\mathbf{C}} \otimes \mathbf{A}) \\ \sqrt{\frac{\alpha_1}{2}} \tilde{\mathbf{L}} \end{bmatrix} \tilde{\mathbf{w}} - \begin{bmatrix} \Sigma^{-\frac{1}{2}} \mathbf{b} \\ \mathbf{0} \end{bmatrix} \right\|_2^2,$$

$$g(\tilde{\mathbf{w}}) = \frac{\alpha_2}{2} [\mathbf{0} \quad \mathbf{1}] (\mathbf{M} \otimes \mathbf{I}) \tilde{\mathbf{w}},$$

439 then we need the smallest Lipschitz constant K for $\nabla f(\tilde{\mathbf{w}})$, which is the largest
 440 eigenvalue for $\nabla^2 f(\tilde{\mathbf{w}})$. That is to say,

$$441 \quad (4.3) \quad K = \lambda_{\max} \left[(\tilde{\mathbf{C}}^T \otimes \mathbf{A}^T) \Sigma^{-1} (\tilde{\mathbf{C}} \otimes \mathbf{A}) + \alpha_1 \tilde{\mathbf{L}}^T \tilde{\mathbf{L}} \right].$$

442 Since we only need the largest eigenvalue, it is not necessary for us to construct
 443 these matrices explicitly; instead we can use an iterative approach, such as the power
 444 method [6]. Note that we only need to calculate K once for all FISTA iterations. The
 details are shown in Algorithm (4.2).

Algorithm 4.2 Power Method [6]

- 1: *Initialization:*
- 2: Generate a random vector \mathbf{q}_0 and normalize \mathbf{q}_0 ;
- 3: **for** $i = 1, 2, \dots$ **do**
- 4: $\mathbf{z}_i = [(\tilde{\mathbf{C}}^T \otimes \mathbf{A}^T) \Sigma^{-1} (\tilde{\mathbf{C}} \otimes \mathbf{A}) + \alpha_1 \tilde{\mathbf{L}}^T \tilde{\mathbf{L}}] \mathbf{q}_{i-1}$;
- 5: $\mathbf{q}_i = \mathbf{z}_i / \|\mathbf{z}_i\|_2$;
- 6: $\lambda_i = \mathbf{q}_i^T [(\tilde{\mathbf{C}}^T \otimes \mathbf{A}^T) \Sigma^{-1} (\tilde{\mathbf{C}} \otimes \mathbf{A}) + \alpha_1 \tilde{\mathbf{L}}^T \tilde{\mathbf{L}}] \mathbf{q}_i$;

445

446 **4.3. Projections.** In addition to the largest eigenvalue, we also need to handle
 447 the linear inequality constraints $(\mathbf{M} \otimes \mathbf{I}) \tilde{\mathbf{w}} \geq \mathbf{0}$. Generally speaking, we can regard
 448 Problem (3.13) as a quadratic programming problem under these specific constraints.
 449 To impose the linear inequality constraints, we can construct another quadratic pro-
 450 gramming problem that offers a nearest solution to satisfy these constraints. If we
 451 assume that we have obtained $\tilde{\mathbf{w}}_k$ in the k -th step, then we build a projection problem
 452 of the form:

$$453 \quad (4.4) \quad \begin{aligned} \min_{\tilde{\mathbf{w}}_{\text{new}}} \quad & \|\tilde{\mathbf{w}}_{\text{new}} - \tilde{\mathbf{w}}_k\|_2^2 \\ \text{subject to} \quad & (\mathbf{M} \otimes \mathbf{I}) \tilde{\mathbf{w}}_{\text{new}} \geq \mathbf{0}. \end{aligned}$$

454 For small and medium size problems, we can solve it efficiently by direct implemen-
 455 tation of standard optimization algorithms. For example, we can use CVX [7, 8]
 456 to solve Problem (4.4), which turns to be low-cost both in storage and calculation
 457 consumptions. However, there are challenges for large-scale problems. For example,
 458 saving long vectors or constructing sparse matrices might require large storage space.
 459 Therefore, we should find a method to decompose Problem (4.4) into small pieces and
 460 try to solve each small problem accurately and efficiently.

461 Suppose we reshape vectors into matrices, for example using MATLAB's "re-
 462 shape" function, $\tilde{\mathbf{W}}_{\text{new}} = \text{reshape}(\tilde{\mathbf{w}}_{\text{new}}, N_v, N_m)$ and $\tilde{\mathbf{W}}_k = \text{reshape}(\tilde{\mathbf{w}}_k, N_v, N_m)$,

463 then by Kronecker product properties and the connection between the 2-norm and
 464 the Frobenius norm, Problem (4.4) is equivalent to

$$465 \quad (4.5) \quad \begin{aligned} \min_{\tilde{\mathbf{W}}_{new}} \quad & \left\| \tilde{\mathbf{W}}_{new} - \tilde{\mathbf{W}}_k \right\|_F^2 \\ \text{subject to} \quad & \tilde{\mathbf{W}}_{new} \mathbf{M}^T \geq \mathbf{0}. \end{aligned}$$

466 If we focus on each row of $\tilde{\mathbf{W}}_k$, $\tilde{\mathbf{W}}_k(i, :)$, then Problem (4.5) can be rewritten as

$$467 \quad (4.6) \quad \begin{aligned} \min_{\tilde{\mathbf{W}}_{new}} \quad & \sum_{k=1}^{N_v} \left\| \tilde{\mathbf{W}}_{new}(i, :) - \tilde{\mathbf{W}}_k(i, :) \right\|_2^2 \\ \text{subject to} \quad & \tilde{\mathbf{W}}_{new}(i, :) \mathbf{M}^T \geq \mathbf{0}, \end{aligned}$$

468 where $\tilde{\mathbf{W}}_{new}(i, :)$ is the corresponding i -th row in $\tilde{\mathbf{W}}_{new}$. It is obvious that this
 469 problem is separable, and the original problem (4.5) can be separated into small-sized
 470 problems that only involve each row of $\tilde{\mathbf{W}}_{new}$ and $\tilde{\mathbf{W}}_k$. Since each row only depends
 471 on the number of materials N_m , then the size of each problem is usually 2×1 or 3×1 .
 472 In this case, we can solve each small-sized problem efficiently and concatenate the
 473 solutions into a large matrix. To realize this idea, we can find a highly efficient solver
 474 for small-sized problems and loop around the number of voxels (pixels if 2D) N_v . In
 475 this paper, we choose CVXGEN [15, 16, 17, 18] to generate a customized solver for
 476 small quadratic programming problems. It is a problem-specific, fast and accurate
 477 code generator which can achieve advance performance in particular for small-sized
 478 quadratic programming problems. In addition, if computer clusters are available, we
 479 can write parallel programming codes, such as MPI or OpenMP, and compute the
 480 solution to this projection problem in parallel. The speedup in this case relies on
 481 the number of available compute nodes, but clearly there is potential for significant
 482 speedup with such an approach.

483 In conclusion, we can see that this algorithm incorporates the advantages of the
 484 power method, FISTA and the fast solver, CVXGEN, for small-sized problems. With
 485 the power method, we only need to save the Hessian-vector multiplication rather
 486 than the full Hessian, and it is very cheap to compute. Moreover, we can achieve
 487 a rapid convergence by FISTA in the main loop. Finally, the projection problem is
 488 decomposed into many small pieces and each can be solved by CVXGEN efficiently.

489 **5. Numerical Experiments.** To test the performance of our preconditioner
 490 and the main algorithm, we set up a test problem that is composed of two materials,
 491 plexiglass and polyvinyl chloride (PVC). The size of each material map is 128×128 .
 492 The first material map is a circular mask that dominates the object, while the second
 493 material map consists of small “spikes” that are scattered randomly inside the circle.
 494 The number of “spikes” is chosen to be 50. Outside of the circle, we assume that
 495 there exist no weights of the object. These two images are shown in Figure 5.1.

496 Inside the mask, the darker blue areas for the first material map are mainly
 497 located in the upper left and lower right corners, which corresponds to blank points.
 498 Other areas inside the circle are represented by heavily weighted yellow and green
 499 color. In the second material map, the weights are scattered around the image and
 500 only occupy a small part of the area in total. This test problem can be regarded as
 501 a simplification of a real life application. For example, in medical imaging for cancer
 502 detection, the first material map is similar to a small area of human body or tissue,
 503 while the second material map can represent the calcium located inside this area.

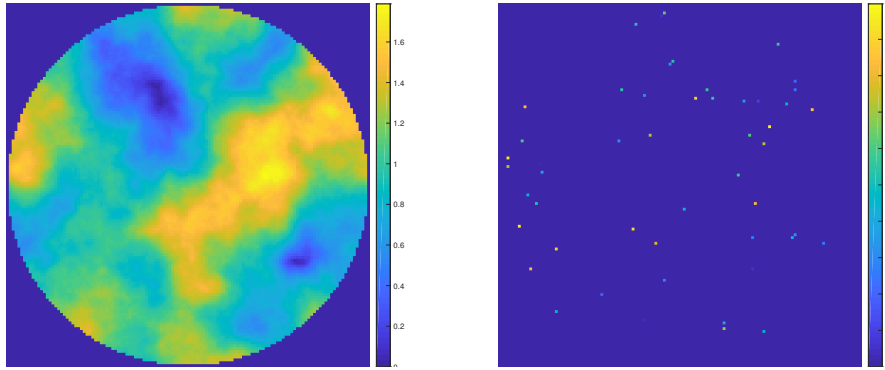


FIG. 5.1. The original material maps for Plexiglass (Left) and PVC (Right).

504 In addition to the test images, we also need other parameters in Equation (1.1). To
 505 generate the ray trace matrix \mathbf{A} , we use the MATLAB function `fanbeamtomolinear`
 506 from AIR Tools [13, 10, 9] to simulate a fan-beam geometry with a flat detector.
 507 Other parameters that we need to choose in this function are presented in Table 5.1.
 In addition, we use 180 projections in total which are equally distributed from 0 to

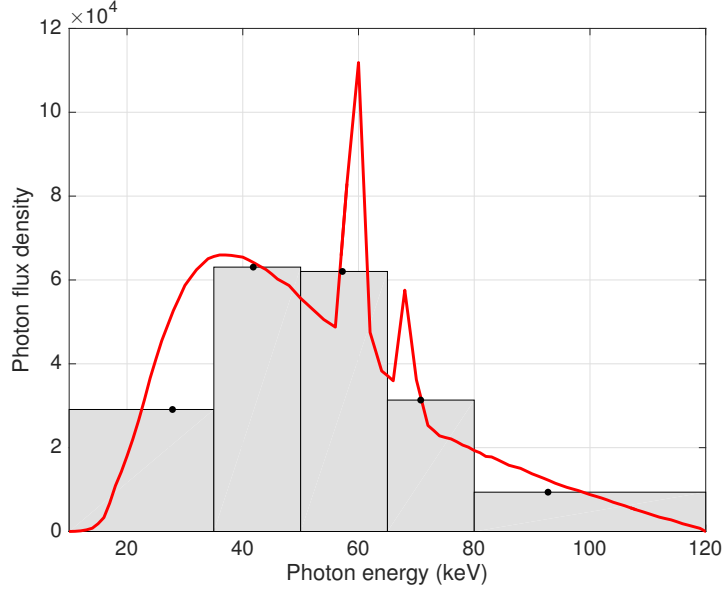
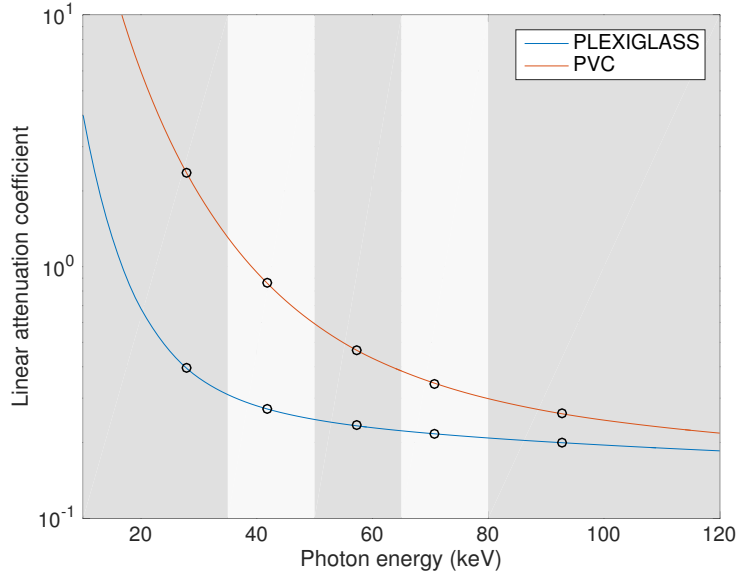
Items	Parameters (cm)
Width of Domain	2.0
Distance from Source to Rotation Center	3.0
Distance from Source to Detector	5.0
Detector Width	4.0

TABLE 5.1
Geometry Parameters of CT Machine

508 360 degrees. The spectral energy of the x-ray source is generated by the MATLAB
 509 function `spektrSpectrum` [22] with 120 keV voltage as input. The detector is assumed
 510 to be photon-counting with 5 energy windows. From the first energy window to the
 511 fifth energy window, we assume that they can detect the range of photon energies 10
 512 to 34 keV, 35 to 49 keV, 50 to 64 keV, 65 to 79 keV and 80 to 120 keV, respectively.
 513

514 The plot of photon flux density versus photon energy is presented in Figure 5.2.
 515 In Figure 5.2, the red curve represents photon intensity of x-ray source and the gray
 516 boxes indicate energy windows of the detector. Moreover, the black dots are the val-
 517 ues of mean photon energy in each energy window. When we build the test problem,
 518 the full energy spectrum and all the corresponding linear attenuation coefficients are
 519 used, while only the mean photon energies and the corresponding linear attenuation
 520 coefficients are applied for reconstruction. As it is well-known, this strategy of gen-
 521 erating data on a finer grid and solve it on a coarser grid is a standard approach to
 522 avoiding what is called the inverse crime.

523 We also plot the curves of linear attenuation coefficients with respect to pho-
 524 ton energy in Figure 5.3. From Figure 5.3, we can see that the slopes of these two
 525 curves are close to each other, which are likely to introduce the collinearity between
 526 coefficients. Moreover, we assume that the entries of the matrix \mathbf{Y} follow a Poisson
 527 distribution, and for large scale problems, from the Central Limit Theorem, the Pois-
 528 son distribution is approximated well by a Gaussian distribution. So the assumption
 529 of Gaussian model is valid.

FIG. 5.2. *Detector bins and photon flux density.*FIG. 5.3. *Linear attenuation coefficients and photon flux density.*

530 The reconstructed images are shown in Figure 5.4. From Figure 5.4, we can see
 531 that we achieve almost perfect separation for these two materials. Moreover, the
 532 reconstructed images have excellent quality in terms of visuality. Both two material
 533 maps are relatively close to the true images. In the first material map, the distribution
 534 of weights is clear to identify. The low intensity pixels are located in the upper left

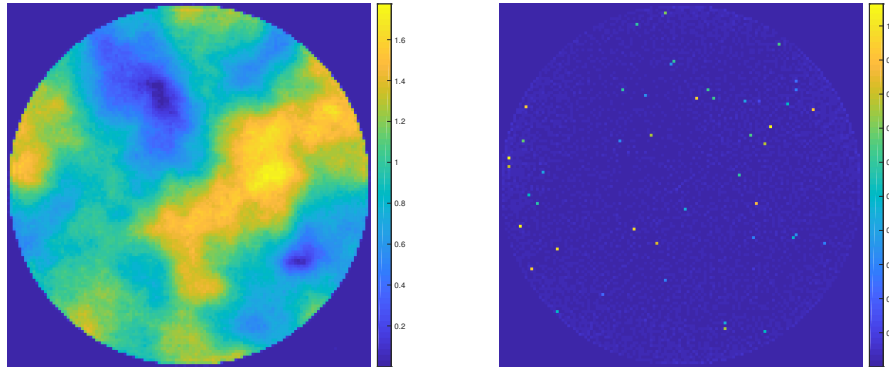


FIG. 5.4. The reconstructed images for plexiglass (Left) and PVC (Right).

535 and lower right areas of the circle, while other places are occupied by the yellow and
 536 green colors. Moreover, we can easily recognize the edges of the circle that indicate
 537 the boundary of the object, which is a plus. As we can see, the reconstruction of
 538 small “spikes” are of great difficulty because of the randomness of weights and spots.
 539 However, we can see that the small “spikes” are scattered in the same positions as
 540 the true image, while they are masked by the shade of a circle. These results present
 541 the significance of methods proposed in this paper.

542 To further validate the results, we plot the relative errors of these two materials
 543 versus the number of FISTA iterations. The decrease of relative errors of corresponding
 544 materials is shown in Figure 5.5. From this figure, we can see that the relative

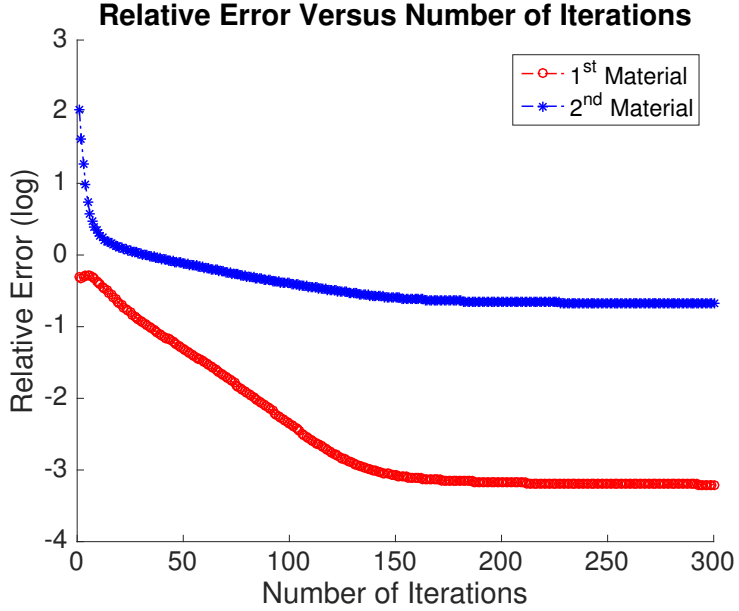


FIG. 5.5. The related errors for each iteration (with preconditioner) for plexiglass and PVC.

544
 545 error of the first material drops sharply as the number of iterations increase. It then
 546 stagnates after around 150 iterations. However, the relative error of the second ma-

547 terial only decreases fast in the beginning, and after several iterations, the rate of
 548 change slows down and the relative error cannot reduce further. We can also iden-
 549 tify the same phenomenon by comparing the true and reconstructed images of the
 550 second material map. Even if the spots of these “spikes” are approximately correct,
 551 the numerical weights of these dots might not be the same. Moreover, there are a
 552 large number of small values in the background of the reconstructed image, causing
 553 somewhat large relative errors, even though visually the result looks quite good.

554 Other accuracy measures illustrate this phenomenon. In Figure 5.6, we plot the
 555 mean squared error (MSE) at each iteration. In Figure 5.7, the structural similarity
 index (SSIM) is presented. Not surprisingly MSE produces information very similar

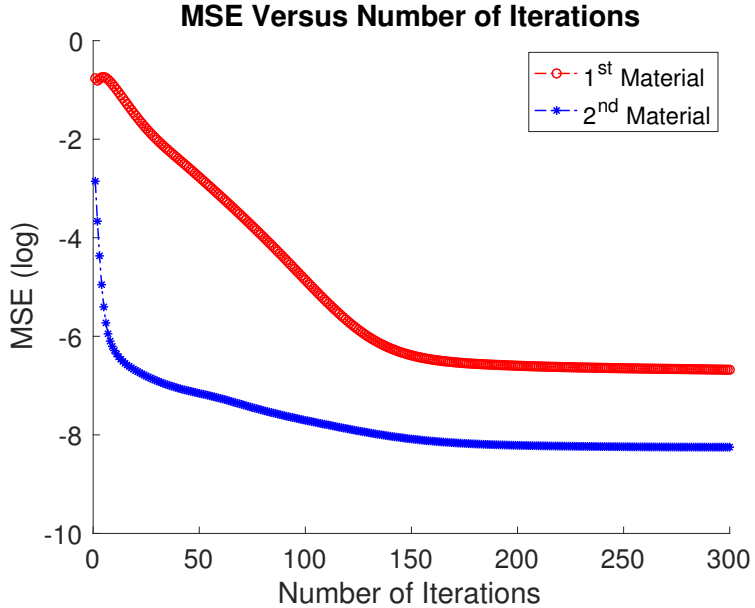


FIG. 5.6. *MSE for each iteration (with preconditioner) for plexiglass and PVC.*

556 to the relative errors, but it also shows a clear diminution for the second material from
 557 Figure 5.6. The SSIM is a metric for image quality and large values correspond to
 558 better solutions. From Figure 5.7, it can be found that the quality of the reconstructed
 559 first material map improves slowly in the early iterations but it achieves a higher
 560 quality measure in the end compared with the second material map. In summary,
 561 all of these errors and quality measures illustrate fast convergence to high quality
 562 reconstructions.

563 It may also be of interest to observe the decay of norm of the gradient at each
 564 iteration, which is shown in Figure 5.8. From this figure, we can see that the norm
 565 of the gradient decreases significantly in the beginning and levels off after a sufficient
 566 number of iterations, indicating the convergence to a minimizer.

567 To further validate the strength of our proposed preconditioner, we compare the
 568 performance with a preconditioner proposed by Barber [1], and the performance with-
 569 out using any preconditioners. As previously mentioned, the approach proposed in
 570 [1] is based on the eigenvalue decomposition of $\mathbf{C}^T \mathbf{C}$. The results are shown in Fig-
 571 ure 5.9, where we plot the decay of relative errors for these three cases. To reduce
 572 clutter in this plot, we only show results for the first material; the behavior for the
 573

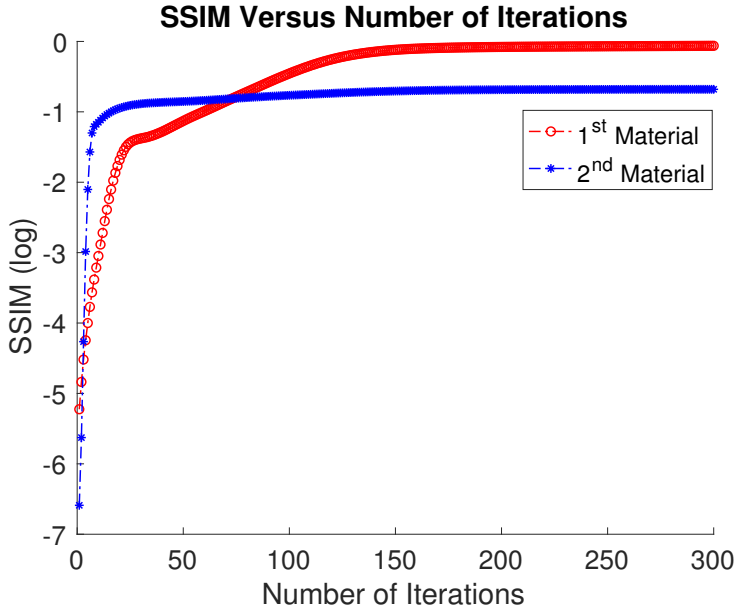


FIG. 5.7. *SSIM for each iteration (with preconditioner) for plexiglass and PVC.*

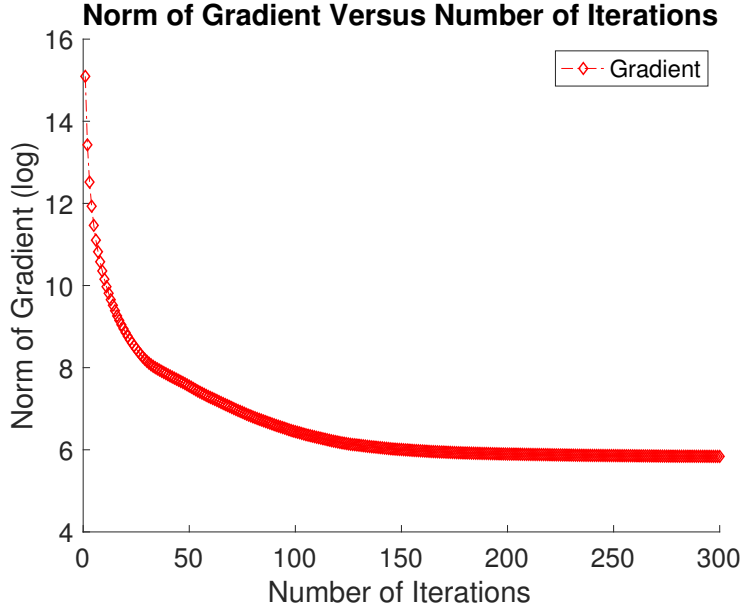


FIG. 5.8. *The norm of the gradient for overall materials, normalized by the 2-norm of the image.*

574 second material is the same. From this figure, we can easily observe that both pre-
 575 conditioners are effective at accelerating convergence, with our approach producing
 576 the fastest convergence and the lowest relative errors.

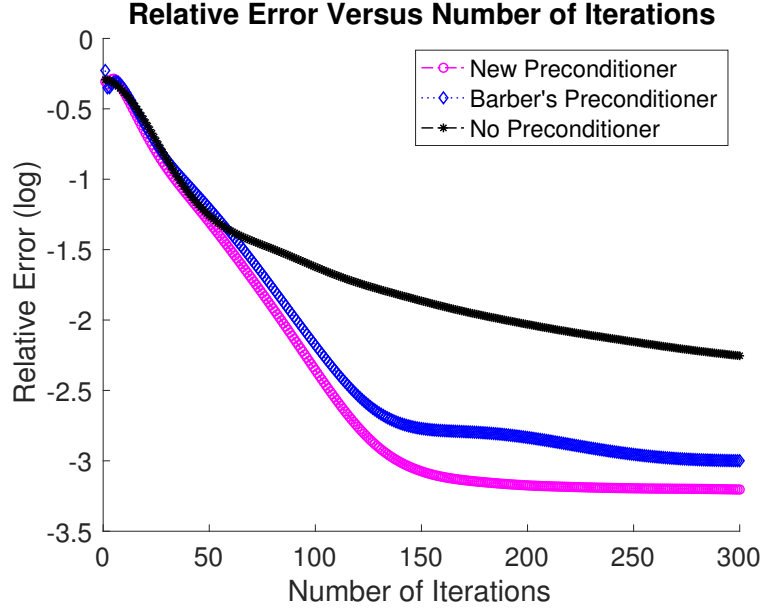


FIG. 5.9. The decay of related errors with new preconditioner, Barber's [1] preconditioner, and with no preconditioner.

577 **6. Conclusions and Remarks.** In this paper, we use the Gaussian assumption
 578 of noise to construct a weighted least squares problem under bound constraints
 579 for energy discriminating x-ray detectors in computed tomography. Based on this
 580 problem, we propose a new preconditioner that includes not only the information of
 581 the linear attenuation coefficient matrix \mathbf{C} but also the projected data matrix \mathbf{Y} and
 582 the energy spectrum matrix \mathbf{S} . With this new preconditioner, the condition number
 583 of the Hessian can be reduced significantly. To implement this new preconditioner
 584 within an optimization framework, we suggest to use a first order method, FISTA,
 585 that can generate fast convergence speed. Because of the introduction of the new
 586 preconditioner, we recommend to construct a projection problem and compute the
 587 nearest step that will satisfy the linear inequality constraints for each iteration. Fi-
 588 nally, numerical experiments also specify the advantages of the method mentioned in
 589 this paper. For future work, it would be interesting to consider other regularization
 590 schemes to emphasize the edges of the object, such as the total variation.

591 **Acknowledgments.** This work is supported by U.S. National Science Founda-
 592 tion under grant no. DMS-1819042. The content is solely the responsibility of the
 593 authors and does not necessarily represent the official views of the NSF.

594

REFERENCES

595 [1] R. F. BARBER, E. Y. SIDKY, T. G. SCHMIDT, AND X. PAN, *An algorithm for constrained one-*
 596 *step inversion of spectral CT data*, Physics in Medicine and Biology, 61 (2016), p. 3784.
 597 [2] A. BECK AND M. TEBOULLE, *A fast iterative shrinkage-thresholding algorithm for linear inverse*
 598 *problems*, SIAM Journal on Imaging Sciences, 2 (2009), pp. 183–202.
 599 [3] A. BJORCK, *Numerical Methods for Least Squares Problems*, vol. 51, SIAM, Philadelphia, PA,
 600 1996.
 601 [4] V. M. BUSTAMANTE, J. G. NAGY, S. S. FENG, AND I. SECHOPoulos, *Iterative breast tomosyn-*

602 *thesis image reconstruction*, SIAM Journal on Scientific Computing, 35 (2013), pp. S192–
603 S208.

604 [5] A. CHAMBOLLE AND T. POCK, *A first-order primal-dual algorithm for convex problems with*
605 *applications to imaging*, Journal of Mathematical Imaging and Vision, 40 (2011), pp. 120–
606 145.

607 [6] G. H. GOLUB AND C. F. VAN LOAN, *Matrix Computations*, vol. 3, JHU Press, MD, 2012.

608 [7] M. GRANT, S. BOYD, AND Y. YE, *CVX: Matlab software for disciplined convex programming*,
609 2008.

610 [8] M. C. GRANT AND S. P. BOYD, *Graph implementations for nonsmooth convex programs*, in
611 Recent Advances in Learning and Control, Springer, 2008, pp. 95–110.

612 [9] P. C. HANSEN AND J. S. JØRGENSEN, *AIR Tools II: algebraic iterative reconstruction methods,*
613 *improved implementation*, Numerical Algorithms, (2017), pp. 1–31.

614 [10] P. C. HANSEN AND M. SAXILD-HANSEN, *AIR Tools: A MATLAB package of algebraic iterative*
615 *reconstruction methods*, Journal of Computational and Applied Mathematics, 236 (2012),
616 pp. 2167–2178.

617 [11] B. J. HEISMANN, B. T. SCHMIDT, AND T. FLOHR, *Spectral Computed Tomography*, SPIE Belling-
618 ham, WA, 2012.

619 [12] J. D. INGLE JR AND S. R. CROUCH, *Spectrochemical Analysis*, Prentice Hall College Book
620 Division, NJ, 1988.

621 [13] A. C. KAK AND M. SLANEY, *Principles of Computerized Tomographic Imaging*, SIAM, Philadel-
622 phia, PA, 2001.

623 [14] R. M. LARSEN, *Lanczos bidiagonalization with partial reorthogonalization*, DAIMI Report Se-
624 ries, 27 (1998).

625 [15] J. MATTINGLEY AND S. BOYD, *Automatic code generation for real-time convex optimization*,
626 Convex Optimization in Signal Processing and Communications, (2009), pp. 1–41.

627 [16] J. MATTINGLEY AND S. BOYD, *Real-time convex optimization in signal processing*, IEEE Signal
628 Processing Magazine, 27 (2010), pp. 50–61.

629 [17] J. MATTINGLEY AND S. BOYD, *CVXGEN: A code generator for embedded convex optimization*,
630 Optimization and Engineering, 13 (2012), pp. 1–27.

631 [18] J. MATTINGLEY, Y. WANG, AND S. BOYD, *Code generation for receding horizon control*, in
632 Computer-Aided Control System Design (CACSD), 2010 IEEE International Symposium on,
633 IEEE, 2010, pp. 985–992.

634 [19] J. L. MUELLER AND S. SILTANEN, *Linear and Nonlinear Inverse Problems with Practical Ap-
635 plications*, SIAM, Philadelphia, PA, 2012.

636 [20] A. S. NEMIROVSKY AND D. B. YUDIN, *Problem Complexity and Method Efficiency in Optimiza-
637 tion*, Chichester: Wiley, 1983.

638 [21] Y. E. NESTEROV, *A method for solving the convex programming problem with convergence rate*
639 *o (1/k^ 2)*, in Doklady Akademii Nauk SSSR, vol. 269, 1983, pp. 543–547.

640 [22] J. H. SIEWERDSEN, A. M. WAESE, D. J. MOSELEY, S. RICHARD, AND D. A. JAFFRAY, *Spektr:*
641 *A computational tool for x-ray spectral analysis and imaging system optimization*, Medical
642 Physics, 31 (2004), pp. 3057–3067.

643 [23] C. F. VAN LOAN, *The ubiquitous kronecker product*, Journal of Computational and Applied
644 Mathematics, 123 (2000), pp. 85–100.

645 [24] V. S. K. YOKHANA, B. D. ARHATARI, T. E. GUREYEV, AND B. ABBEY, *Soft-tissue differentia-
646 tion and bone densitometry via energy-discriminating x-ray microct*, Optics Express, 25 (2017),
647 pp. 29328–29341.